

## Poster #965: Lift in the Vertical Shear of Southerly Jet: A Mechanism of Nocturnal Convection in the Absence of Boundaries

Qi Hu and George Limpert

School of Natural Resources and Department of Earth and Atmospheric Sciences  
University of Nebraska-Lincoln, Lincoln, NE 68583-0987

### 1. Introduction

#### a) Background

The U.S. Great Plains has a peculiar and puzzling diurnal cycle of precipitation during the warm season (May-September): a solitary peak at local midnight to early morning hours (Kincer 1916; Rasmusson 1967; Wallace 1975; Balling 1985). This early morning peak is in contrast to an afternoon peak of precipitation in southeastern U.S. and most land areas in Europe and Asia (e.g., Dai 2001). The diurnal peak of precipitation in the Great Plains was explained by Rasmusson (1967) as being caused by intense convective thunderstorms in local midnight-early morning hours. Subsequent studies (e.g., Wallace 1975; Dai et al. 1999) have elaborated specific details of the nocturnal convection and precipitation. Our recent analysis of the NARR data (Mesinger et al. 2006) from 1981-2010 adds more specifics that the midnight-early morning convective precipitation in the Great Plains contributes to nearly 80% of its convective precipitation in May-September, and about 35% of its total precipitation (Xu 2018). These results show the critical importance of the nocturnal convection and precipitation to severe weather, water resources, as well as the safety and wellbeing of communities in the region.

Progress has been made over the decades in understanding and forecasting the initiation and development of nocturnal convection in the Great Plains. A recent field campaign, the Plains Elevated Convection at Night (PECAN), conducted in June-July 2015, was designed and operated aiming solely at observing details of dynamic and thermodynamic processes evolving during, and supporting the initiation of, nocturnal convection in the Great Plains (Geerts et al.

2017). The process at the focus of PECAN is elevated convection (Corfidi et al. 2008), which accounts for much of the nocturnal deep moist convection. In essence, elevated convection rises in updrafts with inflow originating above the planetary boundary layer (PBL), which becomes shallow and strongly stabilized at night because of surface radiative cooling. Because the origin of convection initiation (CI) is above the PBL, it has been difficult to capture the sources of such CI and to predict convection. There were several instances during PECAN in which all of the model-based convection-allowing simulations failed to forecast pristine CI in the absence of a frontal boundary (e.g., Stelten and Gallus 2017). These instances underscore the need to better understand the mechanisms responsible for nocturnal CI in the Great Plains without air mass boundaries, so forecasts can be improved.

Various sources for elevated convection have been investigated. Recently, Trier *et al.* (2017) have provided evidence suggesting that mesoscale lifting of an elevated moist absolutely unstable layer (MAUL) was a major source of nocturnal CI in several PECAN cases. In this extension of the original conceptual model of a MAUL (Bryan and Fritsch 2000), the requirement of deep and intense lifting in mesoscale complex outflows for MAUL development is relaxed to include weaker ascent motion in mesoscale systems. The ascent motion could be amplified through a positive feedback from the release of convective available potential energy (CAPE) when the MAUL is elevated.

Additional mechanisms of elevated convection have been evaluated, including elevated undular bores propagating on top of a highly stratified nocturnal boundary layer

(e.g., French and Parker 2010; Coleman and Knupp 2011). In those cases, gravity waves in the elevated bores could displace some existing unstable air upward for possible CI (e.g., Marsham et al. 2011). These elevated processes have two roles in nocturnal CI: 1) to overcome low surface-based CAPE in the nocturnal PBL and start convection at elevated levels where instability is sufficient, and 2) to lift, either directly as in the case of a MAUL or indirectly as in bore cases, unstable air to initiate convection.

We note that all these processes for elevated nocturnal CI require the presence of pre-existing air mass boundaries. For example, the formation of a MAUL requires the presence of a front to produce the necessary lifting over a deep layer (Bryan and Fritsch 2000; Trier et al. 2017). Bores can only form along a hydraulic jump, which requires the presence of a front, typically ahead of a cold front (bores forming after a cold front passes are unlikely to cause CI and are not included in this discussion) or in conjunction with outflow from pre-existing convection. In addition, bores leading to CI would require the presence of unstable moist air ahead of the gravity waves, a condition that is unlikely to be present after cold frontal passage. When there is no such boundary, these mechanisms cannot operate. Additionally, in cases of pristine CI, initiation mechanisms are often weak, subtle, and difficult to discern (Stelten and Gallus 2017; Wilson *et al.* 2018). CI is generally better forecasted when larger scale forcing mechanisms are responsible for generating lift (Wilson and Roberts 2006), and are particularly challenging to forecast when CI occurs at a significant distance from any boundary (Stelten and Gallus 2017).

The climatology of strong nocturnal convection in the U.S. Great Plains recently compiled by Reif and Bluestein (2017) reveals that nearly one third of those events initiated without air mass boundaries associated with fronts or mesoscale convection systems (MCS). CI in this group cannot be explained by mechanisms requiring air mass boundaries. Trier et al. (2017)

examined a case without a boundary (July 5, 2015). They used trajectories and showed large-scale advection of warm and moist air active several hours before CI. Large-scale advection has been found to increase CAPE (Zhang 2003), which is enhanced overnight in the Great Plains because of the nocturnal low-level wind maximum in this region. Zhang (2003) showed that on nights when CI occurred, elevated instability generated by large-scale advection has a diurnal peak in local early morning hours, in-phase with the precipitation peak. Stelten and Gallus (2017) propose that the veering of the low-level jet may enhance warm advection during this time, provided there is a zonal temperature gradient, which may explain the secondary peak in nocturnal CI after local midnight. Why does the net positive CAPE generated by large-scale advection not lead to nocturnal convection in models? These results and questions that they raise point to additional processes that can effectively use existing CAPE in nocturnal CI in the U.S. Great Plains.

#### *b) Lift*

The objective of this work is to examine mechanisms that may produce strong and persistent lifting of parcels above the nocturnal PBL to release existing CAPE and initiate deep convection in the absence of pre-existing air mass boundaries. The U.S. Great Plains have two dominant flow regimes during the warm season: westerlies from the Rockies, and the Great Plains low-level jet (GPLLJ). The GPLLJ is a southerly nocturnal wind maximum near the top of the nocturnal PBL that arises from the combination of baroclinity over sloped terrain (Holton 1967) and the inertial oscillation (Blackadar 1957). The result is a supergeostrophic wind maximum with its core typically between 900 -850 hPa and speeds ranging from 10-35  $\text{ms}^{-1}$ . Both these flow regimes intensify at night after their decoupling from surface drag. We propose that the interaction of these two flows produce aerodynamic conditions some of that are conducive to producing lift that is sufficient for nocturnal CI in the absence of

air mass boundaries. These interactions and their potential to generate lift have not yet been examined.

Interactions of the two flow regimes in the Great Plains are analogous to that in fluid mechanics when a laminar flow ( $u$ ) passes a horizontally rotating cylinder. Interactions of horizontally rotating fluid (vortex) around the rotating cylinder with the passing flow (perpendicular to the axis of the vortex) can generate a lift to the horizontal cylinder, as described in the Kutta-Joukowski lift theorem (e.g., Milne-Thompson 1972; Crighton 1985). The lift (force) on the cylinder/vortex is determined by  $L \sim \rho u \omega$ , where  $\rho$  is the density of the fluid. The direction of the lift vector is determined by rotating the wind vector,  $\vec{u}$ , through a right angle opposite to the direction of the circulation,  $\vec{\omega}$  (Milne-Thompson 1972), or,  $\vec{L} \sim \rho \vec{u} \times \vec{\omega}$ . The Kutta-Joukowski lift theorem describes a lift generated by vertical pressure perturbations produced by interactions between a rotating cylinder and a fluid passing it. The rotating body accelerates (decelerates) air passing above (below) the cylinder and produces a negative (positive) pressure perturbation. The result is a vertically-pointing pressure perturbation gradient force that imparts an upward acceleration on the rotating body.

In the Great Plains, the interactions of the two dominant flow regimes in the warm season could produce lift through a mechanism analogous to the process shown in Fig. 1. Although there is no rotating cylinder in the atmosphere to drive a rotating vortex, a horizontal rotation/vortex can rise from the Coriolis' torque on the vertical shear of the southerly winds of GPLLJ. The inertial oscillation (Blackadar 1957), in which Coriolis acts on the supergeostrophic winds within the GPLLJ, causes the GPLLJ to veer and develop a significant westerly component after local midnight. The westerly momentum varies in the vertical direction because of the vertical shear in GPLLJ arising from the

veering wind profile typically associated with warm advection and the supergeostrophic wind speeds within the GPLLJ. The westerly shear below the level of jet core generates a circulation in which air rotates along an axis pointing to the north (the "northern vortex," shown in the yellow cross-section in Fig. 1). Above the core would be a counter-rotating southern vortex. These vortices interact with

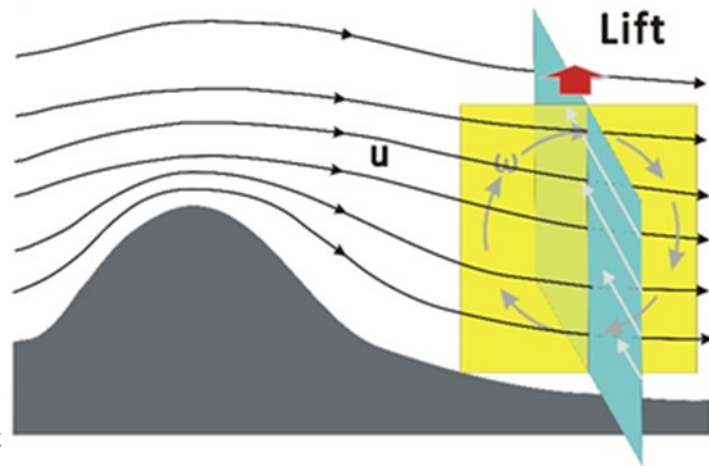


**Figure 1:** A schematic showing the lift analogue to the Kutta-Joukowski lift rising from interactions of the westerly zonal flow ( $u$ ) and a clockwise-rotating vortex ( $\omega$ , on the yellow cross-section) created by Coriolis' torque on low-level southerly flow (on the blue cross-section) in the U.S Great Plains. The bold red arrow is an anticipated lift from interactions of these two flow regimes.

passing zonal westerly winds and could create areas of condition favorable for lift, analogous to that described in the Kutta-Joukowski theorem.

We notice that these northern and southern vortices are coexisting with rotations created *directly* by the vertical shear of the southerly winds in GPLLJ. The rotation below the jet core is along an axis pointing to the west, and an opposite rotation is above the core. These direct vortices interact with the westerly zonal flow as well and result in rather different outcomes (e.g., Wu and Moncrieff 1994; Liu and Moncrieff 1996). The vortex below the jet core is often amplified, whereas the vortex above is suppressed (Fig. 3 in Liu and Moncrieff 1996). This asymmetry also favors ascent of

the vortex below the jet core, which is against the mean zonal flow. Because this ascent, which is on the west side of the GPLLJ, is not where nocturnal convection in the Great Plains has often been observed, i.e., along the east fringe of GPLLJ (e.g., Pu and Dickinson 2014), interactions of these direct vortices with the mean zonal flow would be less likely responsible for nocturnal CI in the Great Plains. In addition, because the vortex above the jet core is suppressed in the presence of westerly zonal flow, we will focus on lift rising from interactions of the northern vortex (below the jet core) and the zonal flow.

We recognize that the interactions of the northern vortex and the westerly zonal flow are not the same as interactions of a laminar flow passing a horizontally rotating cylinder as in the aerodynamics case of the Kutta-Joukowski theorem; we do not intend to prove, or disprove, the validity of the theorem in the atmosphere. Nonetheless, the two share similarities besides a major difference that the northern vortex in our case is not generated by a rotating cylinder but by vertical shear of the GPLLJ. Because of this difference and the complexity of the environment of the northern vortex, the lift in the atmosphere generated from interactions of the vortex and the westerly zonal flow would be anticipated much more complex than predicted in the theorem. Similar complex interactions of horizontal vortices with surrounding mean flows have precedence in the twisting term of the vertical vorticity equation (e.g., Holton and Hakim 2013).

## **2. Cloud/convection model and experimental design**

To examine our proposed lift mechanism and its role in nocturnal CI in the Great Plains, we use the Bryan Cloud Model (CM1; Bryan and Fritsch 2002) to simulate interactions between a westerly zonal flow and 1) a low-level northern vortex, and 2) a low-level westerly jet. Although several sets of simulations were performed with some variations, this section describes the basic configuration of the model and the two types of simulations. The simulations were

conducted in a two-dimensional  $x$ - $z$  plane with no moisture, open east and west lateral boundaries, and a free slip lower boundary. For simulations using temperature profiles from NARR soundings, the model domain in the vertical direction was 15 km. Otherwise, the domain was 10 km deep with potential temperature increasing at a rate of  $3^\circ\text{Kkm}^{-1}$  from 0-8 km, and  $10^\circ\text{Kkm}^{-1}$  from 8-10 km. In addition, simulations were also made using observed temperature profiles of three nocturnal CI events without air mass boundaries. These cases were used to examine the sensitivity of this mechanism to temperature profiles. The vertical grid spacing of the model was stretched, ranging from 100 m in the lowest 3 km to 500 m above 9 km. Most of the simulations were run with a horizontal grid spacing of 500 m and a domain width of 120 km.

For the northern vortex simulations, we describe the northern vortex by introducing a westerly anomaly atop of an easterly anomaly in the model lower troposphere. The westerly anomalies have a peak wind speed at 2.25 km above the ground, and a vertical recession radius of 750 m. Easterly anomalies have the same peak wind speed but at 750 m above the ground and also diminish 750 m away from the peak. These anomalies will be referred to as  $u'$  in the following discussions, and will be added to the mean zonal wind,  $\bar{u}$ , to determine initial total wind at model grid points. In the simulations, no southern vortex is specified above the northern vortex because of the suppressing effect on it from its interaction with the westerly zonal flow (e.g., Liu and Moncrieff 1996). This restriction is released in the next set of jet simulations in which any effect of a southern vortex on the lift is allowed and examined.

The jet simulations are different from the vortex simulations in that no vortices are specified. Instead, westerly anomalies are introduced in the lower model atmosphere. The anomalies have a maximum wind speed at 1.0 km above the ground and decrease quadratically to zero over a vertical distance of 500 m, unless specified otherwise. This

low-level westerly jet describes the outcome of the Coriolis' torque on the GPLLJ. The subsequent (northern and southern) vortices below and above the level of maximum wind in the jet, rising from vertical shear in the wind anomalies, will be naturally described by model dynamics.

### 3. Results

#### a) Results of northern vortex simulations

Figure 2a shows the initial condition for a vortex simulation; a low-level northern vortex was introduced and centered at 1500 m above the ground. Rotation is induced by

northern vortex). Both show ascent in the western half of the northern vortex with peak ascent near the level of the vortex center. The eastern half of the vortex has descent. Near this descent area and on the east side of the northern vortex is a narrow band of strong rising motion. It starts from near the surface and peaks at 2-5 km above the surface. This band of ascent is slanted westward above the vortex and connects with a broad area of ascent over the vortex from 5 km to the top of the model domain. West of this ascent at the same altitude is an area of descent. This profile of vertical motions above the northern

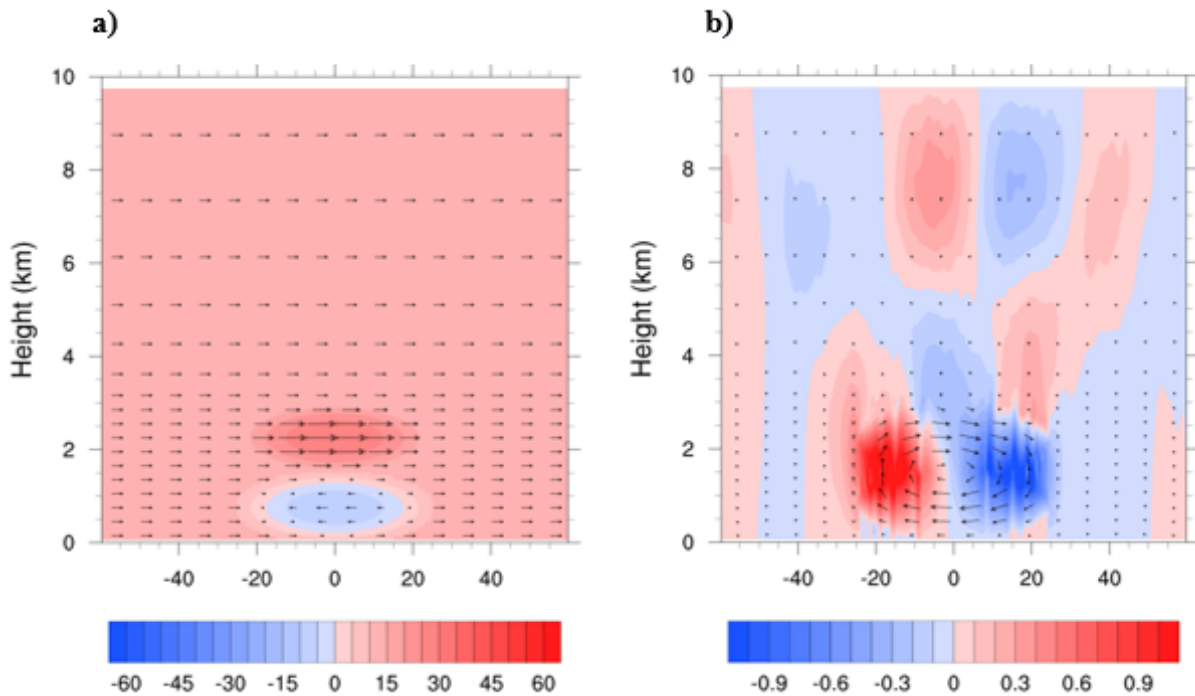


**Figure 2:** a) Initial conditions for the vortex simulation with  $\bar{u} = 10 \text{ ms}^{-1}$  and peak  $|u'| = 20 \text{ ms}^{-1}$ , and b) vertical velocity (units:  $\text{ms}^{-1}$ ) from the vortex simulation at  $t = 300 \text{ s}$  with  $\bar{u} = 0 \text{ ms}^{-1}$  and peak  $|u'| = 20 \text{ ms}^{-1}$ . The northern vortex is shown in this result from imposed initial vertical shear in 2a.

pressure perturbations arising from the conservation of mass, as shown in an example in Fig. 2b. Figure 3 shows the vertical motion field at 1800 seconds from two such simulations. Figure 3a is the result from  $\bar{u}=10 \text{ ms}^{-1}$  and  $|u'|=20 \text{ ms}^{-1}$  for the northern vortex, and Fig. 3b is from  $\bar{u}=10 \text{ ms}^{-1}$  and  $|u'|=8 \text{ ms}^{-1}$  for the vortex (we use absolute values of  $u'$  to indicate maximum speed of eastward and westward flows in the

vortex indicates an extended effect of the interactions of the vortex with the mean flow, as compared with the vertical motion that occurs without a westerly zonal flow (Fig. 2b). Additionally, the horizontal distribution of the vertical motion above 6 km indicates a wave pattern, suggesting vertical propagation of energy from interactions of the northern vortex and the westerly zonal flow. These gravity waves can propagate energy

downwind and provide opportunities for initiation and development of convection outside the vortex area.

Further comparisons of the results in Figs. 3a and 3b, which are from similar runs

develop downward momentum while continuing moving eastward. When reaching the eastern fringe of the vortex, they are further depressed by the sinking motion in the vortex. The parcels rapidly gain positive

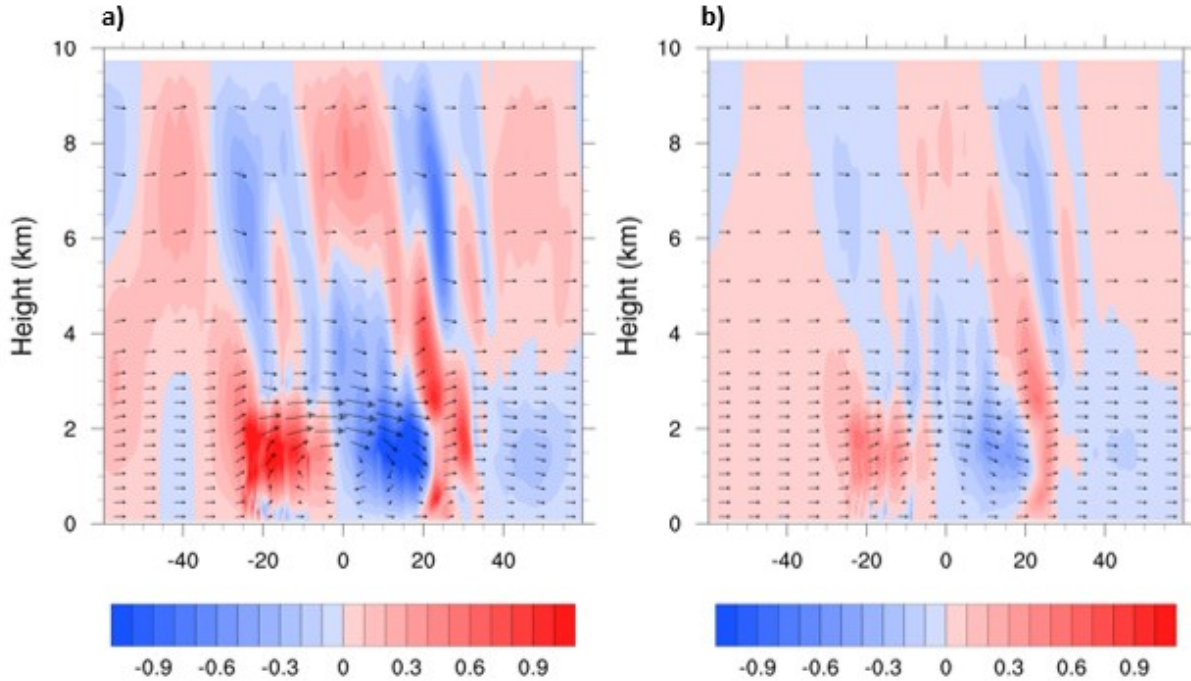


**Figure 3:** Vertical velocity (units:  $\text{ms}^{-1}$ ) from vortex simulations at  $t = 1800$  s with  $\bar{u} = 10 \text{ ms}^{-1}$ , **a)** peak  $|u'| = 20 \text{ ms}^{-1}$ , and **b)** peak  $|u'| = 8 \text{ ms}^{-1}$ .

except for different vortex intensity ( $|u'|$ ) indicate stronger ascent motion and lift when the rotation of the northern vortex is more intense. This result agrees with observations which show that strong nocturnal convection often develops when the GPLLJ (thus the northern vortex in our simulations) is at its strongest (e.g., Higgins et al. 1997).

The lift and vertical motion in Fig. 3 arise from buoyancy generated by interactions of the northern vortex and the westerly zonal flow. Such a buoyancy profile is shown in Fig. 4 for the case shown in Fig. 3a. At 1800 s of simulation, air parcels travelling eastward and entering the northern vortex are mechanically elevated by the rising motion along the western fringe of the northern vortex. The elevated parcels become negatively buoyant when they ascend. While gaining negative buoyancy, these parcels

buoyancy within the strong mechanical descent on the eastern flank of the vortex. Upon being advected east of the downward forcing, the strong positive buoyancy results in rapid ascent and a band of strong upward motion along the eastern fringe of the vortex. When the parcels are lifted they again become negatively buoyant. The asymmetry of the perturbation vertical motion on the western and eastern half of the northern vortex and its interaction with the westerly zonal flow are essential for the intense ascent on the east fringe of the vortex shown in Figs. 3a and 3b.

It is also important to note the concentration of positive buoyancy in the upper atmosphere of the model over the northern vortex (Fig. 4). This result indicates that the source of the gravity waves in the upper layers of the model (Figs. 3a and 3b) is

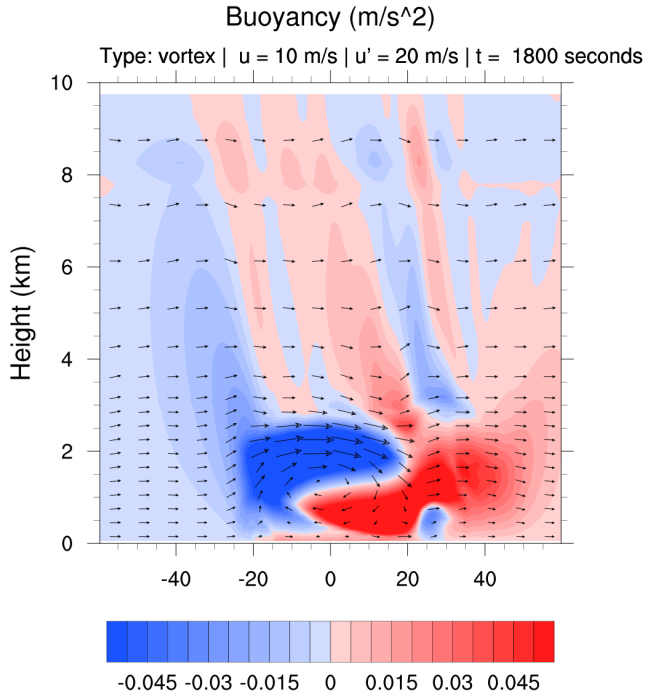


**Figure 4:** Parcel buoyancy (units:  $\text{ms}^{-1}\text{s}^{-1}$ ) in the vortex simulation at  $t = 1800$  s with  $\bar{u} = 10 \text{ ms}^{-1}$  and peak  $|u'| = 20 \text{ ms}^{-1}$ .

on the parcels, previously acquired upward momentum carries them past their original level. In some of the simulations, the upward motion at the eastern fringe of the vortex reaches  $1.0 \text{ ms}^{-1}$ . This large upward motion of parcels could be partially due to the small horizontal scale of the vortex in our simulation which leads to stronger divergence and pressure perturbations (Fig. 5f) than what may be expected in more realistic atmospheric conditions. Albeit a potentially exaggerated magnitude of the ascent, the area of relatively strong ascent along the eastern fringe/periphery of the low-level southerly jet in the simulations is consistent with the typical location of CI with respect to GPLLJ (e.g., Pu and Dickinson 2014).

The importance of interactions of the westerly zonal flow and the southerly GPLLJ in

over the vortex area.

Further details of these processes are provided in Fig. 5 with an example of the Lagrangian path of massless parcels moving through and over the northern vortex. As shown in Figs. 5b and 5e, in simulations with a sufficiently strong westerly zonal flow, parcels that have been mechanically forced downward on the eastern half of the vortex gains positive buoyancy while continuing eastward. As the downward mechanical forcing is relaxed as the parcels reach the east fringe/periphery of the vortex, they ascend rapidly. Although the fast ascent eventually imposes negative buoyancy

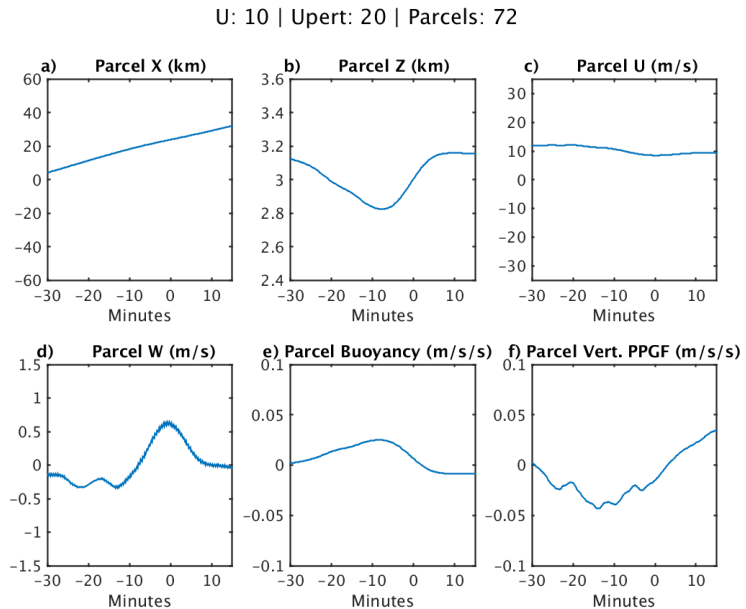


**Figure 5:** Average parcel trajectories for parcels ascending through an area 20-30 km east of the vortex center, 3.0 km above ground level, during the period from 1800-3600 s into the simulation. Time of zero is when the parcel first ascends through the aforementioned area after entering it. This is from simulation with  $\bar{u} = 10 \text{ ms}^{-1}$  and  $|u'| = 20 \text{ ms}^{-1}$ .

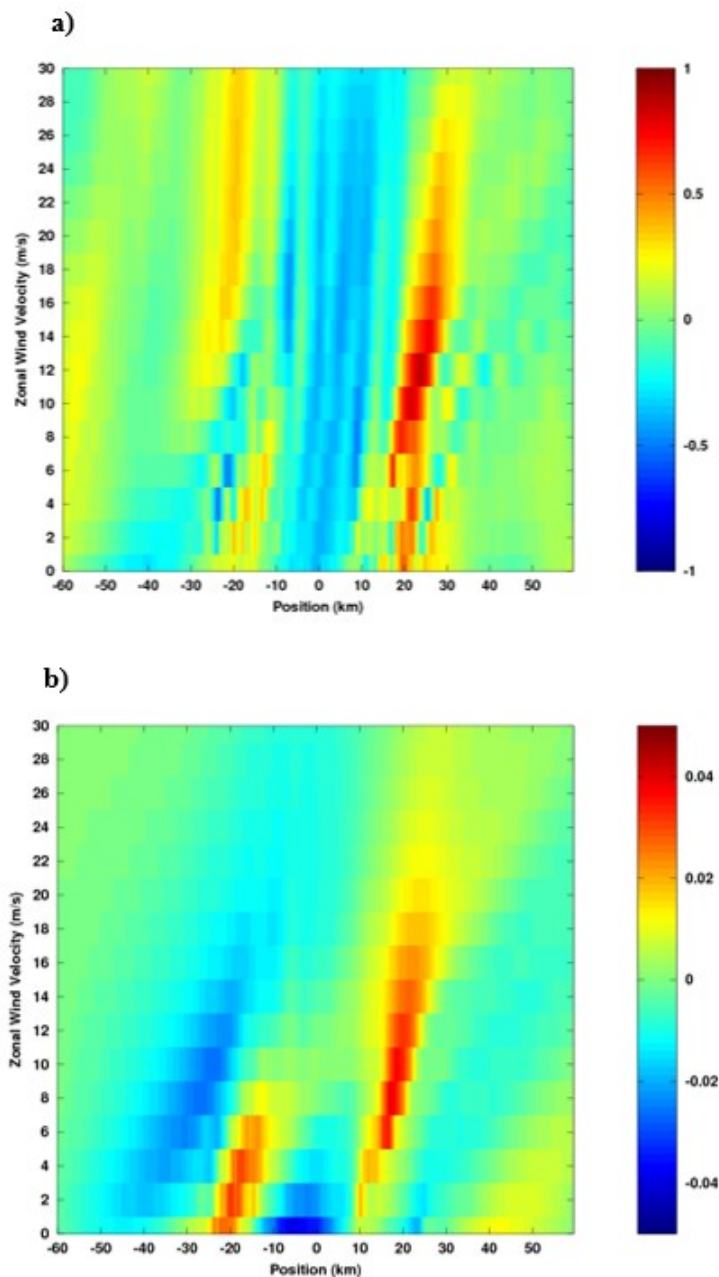


**Figure 6:** **a)** Vertical velocity (units:  $\text{ms}^{-1}$ ) at 3.0 km above ground level averaged over 1800-3600 s into simulations which used different zonal westerly wind speed (0 to  $30 \text{ ms}^{-1}$ ) and a fixed  $|u'| = 20 \text{ ms}^{-1}$ . The horizontal axis is the  $x$ -position within the domain, and  $x=0$  is the center position of the northern vortex. **b)** Similar to a) but for parcels buoyancy (units:  $\text{ms}^{-1}\text{s}^{-1}$ ) at 3.0 km above the ground.

ascent and nocturnal CI is further evaluated with simulations using different zonal westerly wind speeds. Figure 6a summarizes

the results for vertical motion at 3 km above the ground level. At the specified  $|u'| = 20 \text{ ms}^{-1}$ , Fig. 6a shows strong upward motion from  $0.5\text{-}1.0 \text{ ms}^{-1}$  in a 5-8 km wide band at 20-25 km east of the center position of the northern vortex (equivalent to the GPLLJ core longitude) when  $\bar{u}$  is  $6\text{-}18 \text{ ms}^{-1}$ . The upward motion peaks at  $\bar{u} = 12 \text{ ms}^{-1}$ . Ascent weakens for stronger  $\bar{u}$  ( $>20 \text{ ms}^{-1}$ ). For weaker  $\bar{u}$  ( $<5.0 \text{ ms}^{-1}$ ), ascent is confined in narrower bands and less organized.

Parcel buoyancy at the same level (3.0 km) is shown in Fig. 6b. It has a similar distribution to the vertical motion in Fig. 5a. Strong positive buoyancy occurs along the eastern fringe/periphery ( $\sim 15\text{-}20 \text{ km}$  from the center position) of the northern vortex when  $\bar{u} = 5\text{-}18 \text{ ms}^{-1}$ . Over the vortex at this level is weak positive buoyancy. When  $\bar{u}$  strengthens ( $>20 \text{ ms}^{-1}$ ), the areas of buoyancy become blurred and weaker, likely due to the decreased residence time that parcels spend within an area of mechanical ascent or descent and, therefore, acquire less positive or negative buoyancy along their trajectories.

For  $\bar{u} < 5 \text{ ms}^{-1}$ , positive buoyancy is found on the western side of the vortex center. This location of positive buoyancy and ascent (Fig. 6a) in weak  $\bar{u}$  cases is explained because parcels entering the vortex area at this level (3 km) from the west are pressed downward into the lower levels where divergence takes place along the western edge of the vortex, owing to an increase in westerly flow by the rotation of the vortex.

The forced descent causes parcels to acquire positive buoyancy upon moving to levels of lower potential temperature.

Although different from a single lift

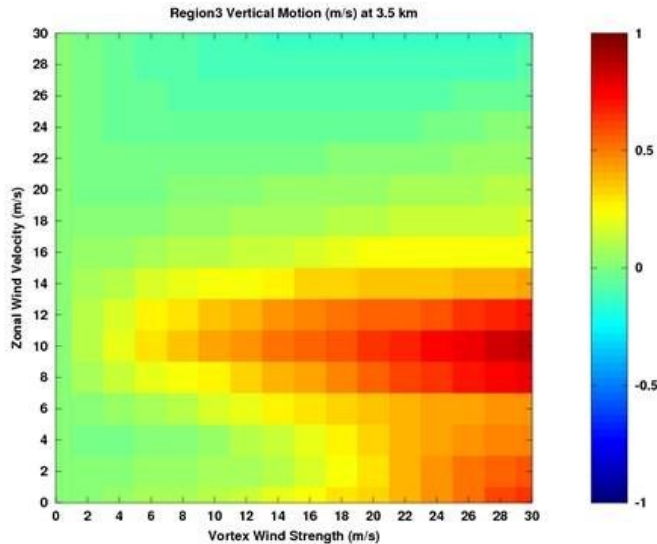


**Figure 7:** Vertical velocity (units:  $\text{ms}^{-1}$ ) at 3.0 km above ground level averaged over 1800-3600 seconds into the simulation and in the region 18-25 km east of the vortex center. The result shows that a stronger northern vortex would favor stronger upward motion for westerly zonal wind 7-15  $\text{ms}^{-1}$ .

on a solid rotating cylinder as in the Kutta-Joukowski theorem in aerodynamics, these buoyancy profiles and related vertical motion fields in our simulations portray a collective lift of the northern vortex. As shown in Figs. 3-6, positively buoyant parcels are in the lower half of the vortex (Fig. 4). Mechanically forced parcels ascend above and on the western half of the vortex (Fig. 3), although those parcels soon gain negative buoyancy upon overshooting their original level. Bands of strong ascent are on the east fringe and periphery of the vortex (Figs. 3 and 6). The collective lift is further ratified by the positive buoyancy and upward motion *above* the northern vortex (Figs. 3, 4, and 6) where because only westerly zonal flow is present the strong ascent is only possible from upward momentum originating from the interactions of the two flow regimes in the lower troposphere.

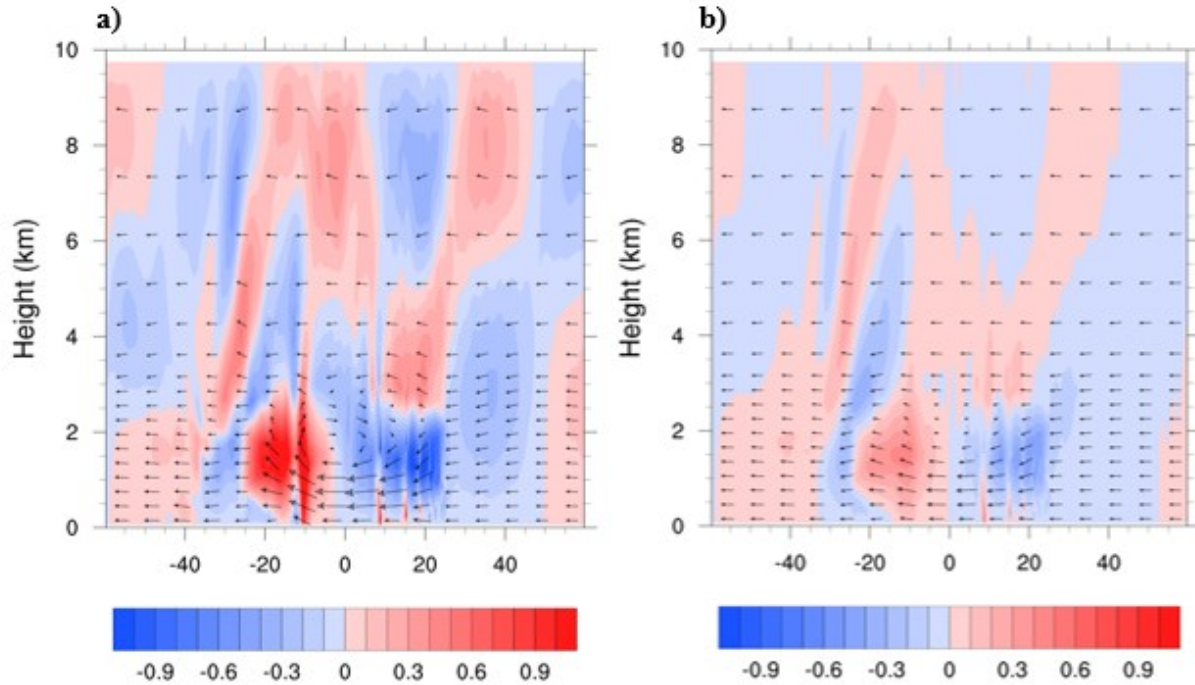
We have also examined how these results would change in a mean easterly zonal flow ( $\bar{u} < 0$ ). Figure 8 shows a pair of results from vortex simulations that used  $\bar{u} = -10 \text{ ms}^{-1}$ . The other parameters in these simulations are the same as the ones shown in Fig. 3.

Figure 8 shows descent motion on the east half of the vortex and ascent on the west half. The pattern is similar to Fig. 3, which has a westerly zonal flow. This similarity between the two simulations suggests a dominant role of the rotating vortex on the vertical motion inside it. Outside the vortex, the bands of strong ascent motion along the eastern fringe of the vortex and extending into the upper troposphere in simulations with  $\bar{u} > 0$  (Fig. 3) are absent in simulations with  $\bar{u} < 0$  (Fig. 8), though similar bands are present on the western periphery under these conditions. This difference indicates that the rising motion on the east side of the northern vortex is an outcome of interactions between the vortex and the westerly zonal flow. Another difference between the results in

Figs. 8 and 3 is that the vertical motion in Fig. 8 is less organized than in Fig. 3, suggesting a mean easterly zonal wind as a less likely solution for CI on the eastern flank of the vortex. We will focus on results of simulations using westerly zonal winds in the remaining sections.

#### *b) Results of jet simulations*

As discussed in section 2, the jet simulation is a relaxation of the vortex simulation in the sense that, instead of specifying and varying a northern vortex, we allow model dynamics to generate any vortices around a low-level westerly jet. In this section, we discuss results of such simulations that use low-level westerly perturbations representing the outcome of eastward deflection of the GPLLJ by Coriolis force. Figure 9 shows an example of initial wind profile used in the jet simulations. In all jet simulations, the core (jet) of the westerly wind perturbations is placed at 1000 m above the ground. Perturbation winds of the jet diminish upward and downward to zero in 500 to 1000 m, which will be referred to as “decay distance.”



**Figure 8:** Vertical velocity (units:  $\text{ms}^{-1}$ ) from the vortex simulation at  $t = 1800$  s into simulations with  $\bar{u} = -10$   $\text{ms}^{-1}$ , **a)** peak  $|u'| = 20$   $\text{ms}^{-1}$ , and  $\text{ms}^{-1}$  peak  $|u'| = 8$   $\text{ms}^{-1}$ .

Figures 10a and 10b show vertical motions from a pair of jet simulations at  $t = 1800$  s in simulation using a decay distance of 1000 m and 500 m, respectively. In both simulations, there is initially a negative pressure perturbation on the western side of the jet and positive pressure perturbation on the eastern side, consistent with the pattern of convergence and divergence created by the westerly wind perturbation. Additionally, a positive pressure perturbation develops above the jet ( $\sim 2000$  m above ground level) and becomes stronger later in the simulations. These nonhydrostatic pressure perturbations result in downward mechanical forcing over the western half of the jet. Some parcels that descend on the western periphery of the jet are accelerated through the jet.

As with the vortex simulations, these parcels acquire positive buoyancy as they are mechanically forced downward. Parcels above the jet appear to be ascending into an area with a higher pressure perturbation, that is, they seem to be ascending despite a

downward pressure perturbation gradient force. This suggests that the ascent in this region is primarily the result of buoyancy. However, parcels east of the jet experience an upward pressure perturbation gradient force and, in addition to having acquired positive buoyancy through prior mechanically forced descent, ascend rapidly. In this region, the mechanical forcing and positive buoyancy both contribute to ascent. The ascending motion is stronger in Fig. 10a than Fig. 10b, a result indicating a deeper westerly jet would favor stronger interaction of these processes. These processes are also supported by an analysis of parcel trajectories (Fig. 11), focused on an area 20-30 km east of the core of the westerly wind perturbations and 2 km above ground level.

The parcel trajectories shown in Fig. 11, as well as Fig. 5, have a strong similarity to those calculated by Trier et al. (2017). Their results show parcels descending over the low-level jet, then rapidly ascending as they move eastward. Trier et al. (2017) do not

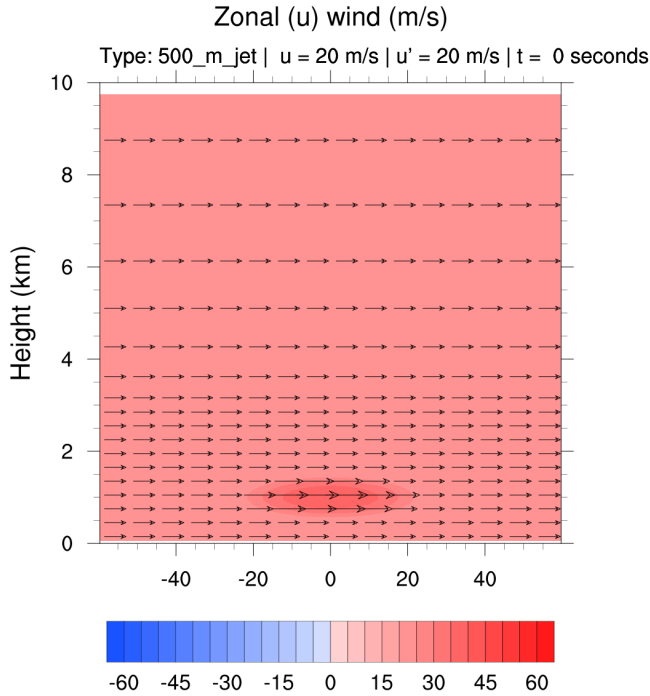


**Figure 9:** Initial conditions for the jet simulation where  $\bar{u} = 20 \text{ ms}^{-1}$  and peak  $u' = 20 \text{ ms}^{-1}$  at 1.0 km. Similar profiles are imposed in simulations using different values of  $\bar{u}$ ,  $u'$ , and the elevation of the jet core.

suggest a mechanism to explain their parcel trajectories. Given that those trajectories are consistent with ours in Fig. 11, the results of Trier et al. (2017) could imply the aforementioned processes at work in nocturnal CI. Specifically, downward mechanical forcing displaces parcels downward from their original level, causing them to acquire positive buoyancy. The westerly momentum eventually carries the parcels past the downward mechanical forcing and above strong convergence on the eastern fringe of the westerly jet. In this region, parcels ascend, driven by both positive buoyancy that was acquired during their descent and the nonhydrostatic vertical pressure perturbation gradients associated with convergence in that area.

We notice that the vertical motion in these simulations is an order of magnitude stronger than in the parcel trajectories calculated by Trier et al. (2017). This

difference is largely because of the concentrated scale of the westerly wind perturbations (westerly jet) in our simulations. In our idealized cases, the scale of the jet is much smaller than in the real cases, thus generating stronger pressure perturbations and subsequently stronger vertical motion. In additional simulations, we kept the model grid spacing unchanged but increased the horizontal width of model domain to allow a stretched westerly jet from the original 60 km to 300 km. This change decreased the magnitude of the pressure perturbation and the resulting vertical velocity, which is consistent in magnitude with that in Trier et al. (2017).

The results from the above comparisons indicate that the scale, both horizontal and vertical, and morphology of the westerly jet will affect vertical motions from interactions of the jet with the westerly zonal flow. These results also raise a question if the model

grid resolution may affect the outcome vertical motion by describing additional details of a jet after its scale, morphology, and strength have been specified. To answer this question, we conducted a set of simulations with a horizontal grid spacing of 4 km (from 500 m in previous runs), similar to the configuration of currently operational convection-allowing models (e.g., Stelten and Gallus 2017). The horizontal length of the jet remained at 25 km, but the domain was expanded to 480 km across. The vertical velocities of these simulations remain nearly the same as in the simulations with 500 m resolution. These comparisons suggest that increasing the resolution of models would not likely solve the problem of WRF having difficulty with nocturnal CI without boundaries. This result is in agreement with recent findings of Thielen and Gallus (2019) who showed that changing the horizontal grid spacing from 3 km to 1 km does not affect the

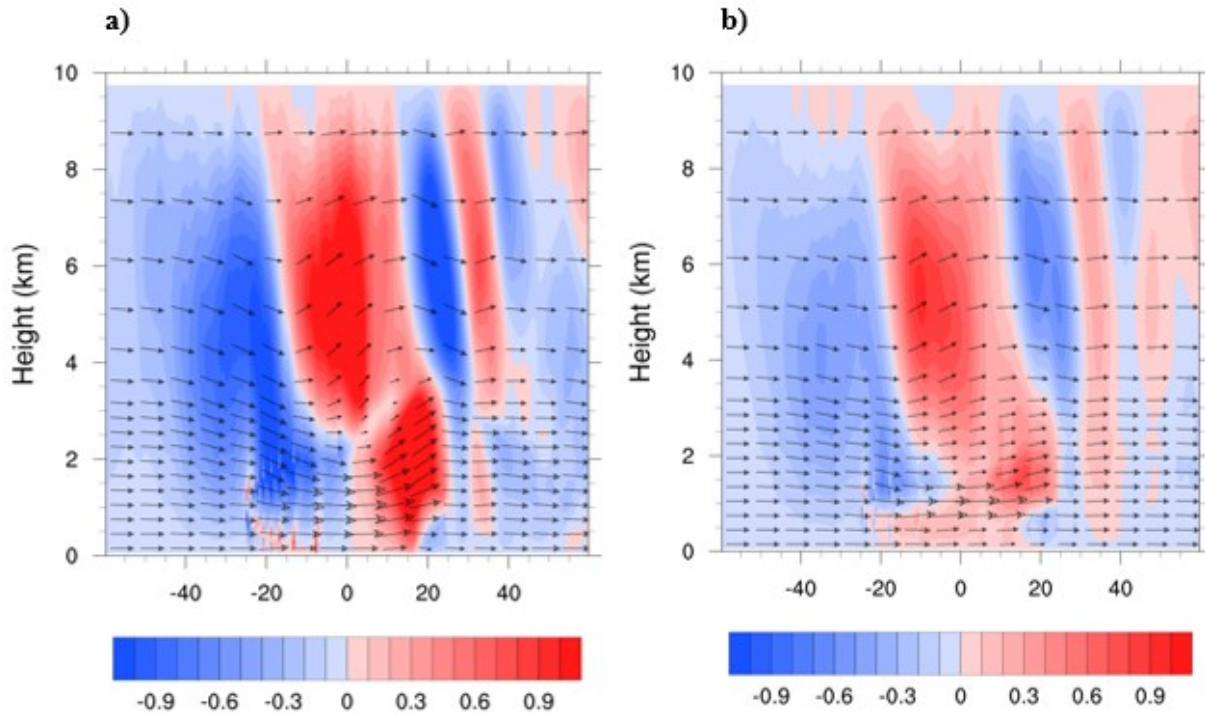


**Figure 10:** **a)** Vertical velocity (units:  $\text{ms}^{-1}$ ) from a jet simulation at  $t = 1800$  s with  $\bar{u} = 20 \text{ ms}^{-1}$  and peak  $u' = 20 \text{ ms}^{-1}$  the decay distance of 1000m. **b)** Same as a) but from simulation at  $t = 2700$  s into the simulation with  $\bar{u} = 20 \text{ ms}^{-1}$  and peak  $u' = 20 \text{ ms}^{-1}$  for the decay distance of 500 m. Vertical motion profile for case b) at  $t = 1800$  s is similar to that shown in b) but less intense, indicating amplifying vertical motion as interactions between the westerly zonal flow and the low-level jet.

vertical velocity enough to explain the difficulty of forecast models to simulate nocturnal pristine CI.

Another interesting feature in Fig. 11 is that the parcels have sustained upward motions while travelling on the eastern side of the westerly jet (from  $t = -16$  to  $t = 0$ ). The buoyancy supporting the lift is gained when the parcels are mechanically forced downward below their original level on the western side of model domain (Fig. 11b) where divergence is created at the level of the jet core. Similar processes are found also developing above the jet at higher altitude where the higher stratification apparently favor stronger and quick lift and ascent (Fig. 10).

This process is largely invariant in a wide range of mean zonal flow conditions from  $5 \text{ ms}^{-1} < \bar{u} < 30 \text{ ms}^{-1}$ , as indicated by the results in Fig. 12a which used a fixed  $u' = 20$

$\text{ms}^{-1}$ . The results show a rather steady pair of bands of vertical motion straddled over the center of the jet; one band of descent is  $\sim 15$ - $20$  km west of the domain center, with a band of ascent  $\sim 15$ - $20$  km east of the jet center. With weak zonal winds of  $\bar{u} < 5 \text{ ms}^{-1}$ , the results suggest disorganized buoyancy processes and vertical motion structure.

Additional simulations show that for  $\bar{u} > 5 \text{ ms}^{-1}$ , increasing the jet speed would result in greater buoyancy of parcels on the eastern side of the jet and subsequently stronger ascent (Fig. 12b). A stronger jet would generate larger mechanical forcing, resulting in stronger buoyancy/lift for the parcels, as previously discussed. Meanwhile, according to the result of Fig. 12b, stronger mean zonal flow would help start this buoyancy-generation process with a weaker jet, although very strong zonal wind also shortens the residence time of parcels in the

U: 20 | Upert: 20 | Parcels: 93

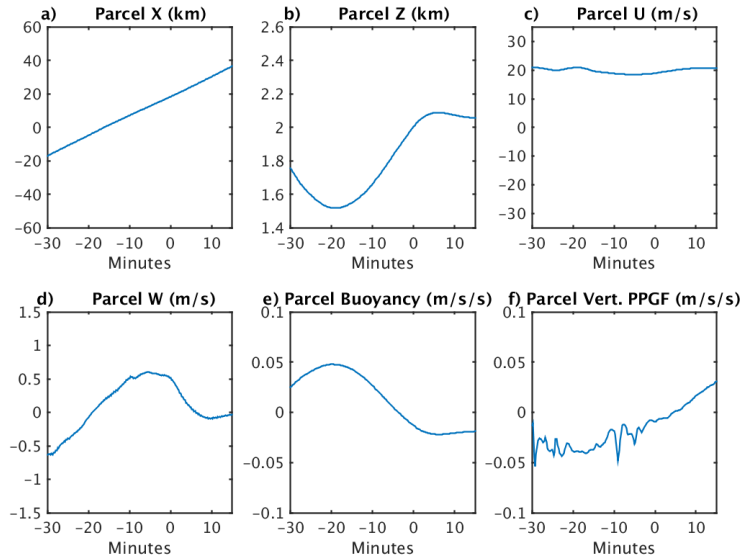


**Figure 11:** Average trajectories for parcels ascending through an area 20-30 km east of the low-level jet center, 2.0 km above ground level, during the period from 1800-3600 s into the simulation. The decay distance of the jet is 500 m. Time of zero is when parcels first ascend through the aforementioned area after entering it. This figure is for  $\bar{u} = 20 \text{ ms}^{-1}$  and  $u' = 20 \text{ ms}^{-1}$ .

jet region and hence weaken the ascent.

### *c) Differences and similarities between the results of the vortex and jet simulations*

The results of the vortex simulations have a pair of sinking and rising motions associated with the vortex rotation, and a band of rising motion around the eastern fringe/periphery of the vortex (Fig. 3). On the west side of the vortex is a pool of weak rising or sinking motion, the direction of vertical motion depending on the strength of the mean zonal flow and the rotation of the vortex. However, the results of the jet simulations have a pair of areas of rising and sinking motions within the width of the westerly jet, but in a sequence opposite to that inside the northern vortex (cf. Figs. 10 and 3). Outside this pair, vertical motions are weak and the direction is also dependent on the strength of the mean zonal flow and the westerly perturbation.

In the mid- and upper troposphere, the jet simulations show strong ascent over the jet

(Fig. 10). However, the vortex simulations show descent stretching to the mid-troposphere on the eastern half of the vortex beneath ascent in the upper troposphere. This ascent is a continuation of slanted bands of rising motion on the eastern fringe of the vortex (Fig. 3). Also shown in Fig. 3 is a wave pattern across the entire model domain in the upper troposphere. Such a wave pattern is not shown in jet simulations (Fig. 10). Instead, the alternation of weak rising and sinking motions in the upper troposphere in Fig. 10 suggests a series of short and fast waves emanating downstream from the center of westerly wind (energy) perturbations in the lower

troposphere. These differences in motion in the upper troposphere are outcomes of interactions of lower troposphere energy disturbances and the upper troposphere flow (e.g., Holton and Hakim 2013). It is interesting that these outcomes are different dependent on the configuration/morphology of disturbances in the lower troposphere.

Although these differences exist, both the vortex and jet simulations produce strong ascent on the eastern flank of the jet/vortex. Parcel trajectory analysis indicates similar processes responsible for the ascent in both vortex and jet simulations. The primary difference in the mechanism between the jet and vortex simulations is that vertical pressure perturbations on the eastern periphery of the jet produce an upward acceleration, whereas in the vortex simulations, the vertical pressure perturbations impart a downward acceleration opposite of the buoyant acceleration. In the vortex simulations, westerly momentum must carry parcels past the downward mechanical

forcing, after which the positive buoyancy accelerates parcels upward. Additionally, the simpler configuration of low-level westerly disturbances in the jet simulations may contribute to greater areal extent and strength of the ascent than the simulations in which the vortex is directly imposed. Both the vortex and jet simulations produce strong ascent in the atmosphere above the jet or vortex, a result demonstrating a collective lift resulting from interactions of the westerly zonal flow and the perturbations of forms of either a northern vortex or a jet.

*d) Simulations with observed temperature soundings*

Three additional sets of simulations were performed using observed temperature profiles from nocturnal CI cases. Two cases occurred during PECAN IOPs on 1) 04 July 2015 at 06 UTC at 37.92°N and 100.22°W (Wilson et al. 2018), and 2) 06 July 2015 at 03 UTC at 40.75°N and 96.5°W (Stelten and Gallus 2017). The third case occurred shortly after the PECAN campaign on 28 July 2015 at 06 UTC at 40.2°N and 97.6°W (Stelten and Gallus 2017). All three have pristine CI away from pre-existing air mass boundaries. Case 1 occurred with relatively weak low-level southerly flow while cases 2 and 3 occurred with significantly stronger GPLLJ. The potential temperature profiles,  $\theta(z)$ , of these cases are shown in Fig. 13, acquired from North American Regional Reanalysis data near the location of CI prior to its occurrence. These profiles have strong inversions in the lowest few hundred meters.

Above the inversion layer, the profiles are statically stable with  $\theta(z)$  increasing at nearly 4°K per kilometer. This strong static

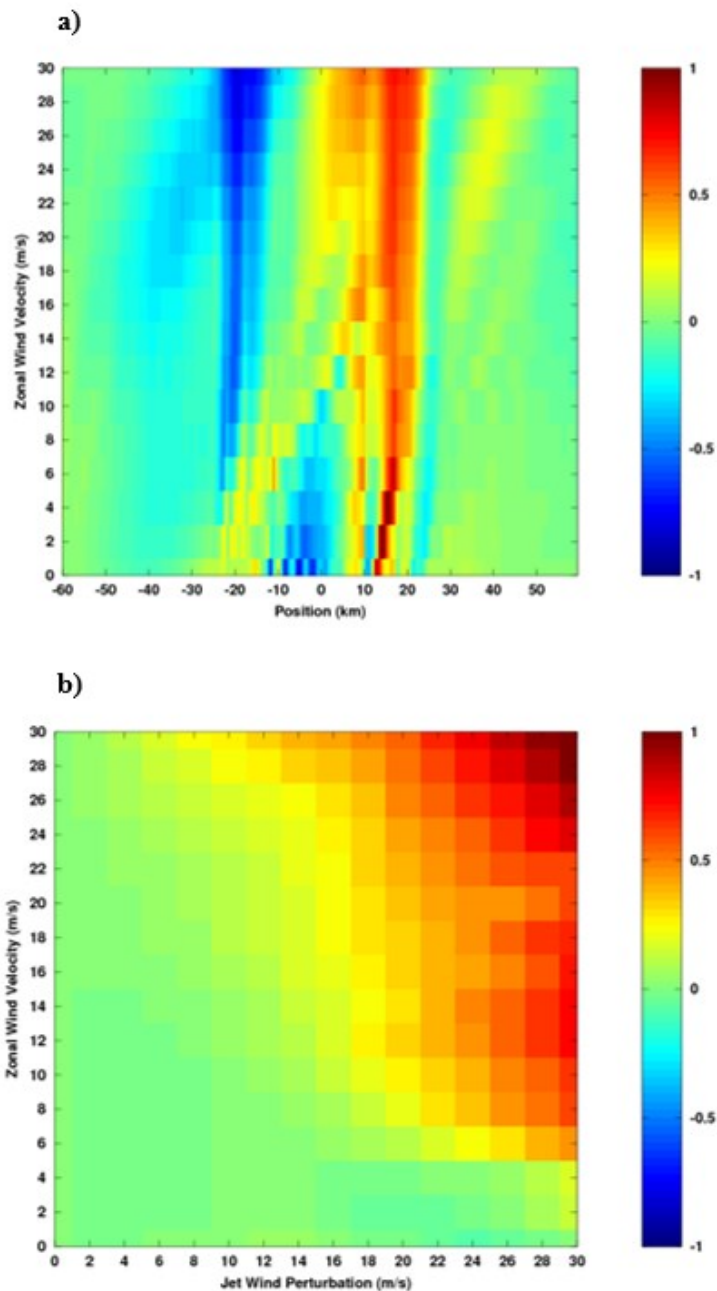


**Figure 12:** **a)** Vertical velocity (units:  $\text{ms}^{-1}$ ) at different distance from the center of model domain (abscissa), measured at 2 km above the ground level, as a function of  $\bar{u}$  (ordinate) at a fixed  $u' = 20 \text{ ms}^{-1}$ . The decay distance of the jet is 500 m. **b)** Vertical velocity (units:  $\text{ms}^{-1}$ ) at 2.0 km above the ground level averaged over 1800-3600 seconds into model simulation in the region 10-20 km east of the model domain center and 2 km above the ground level.

stability at local night hours favors an intense GPLLJ and low-level westerly wind perturbations arising from the inertial

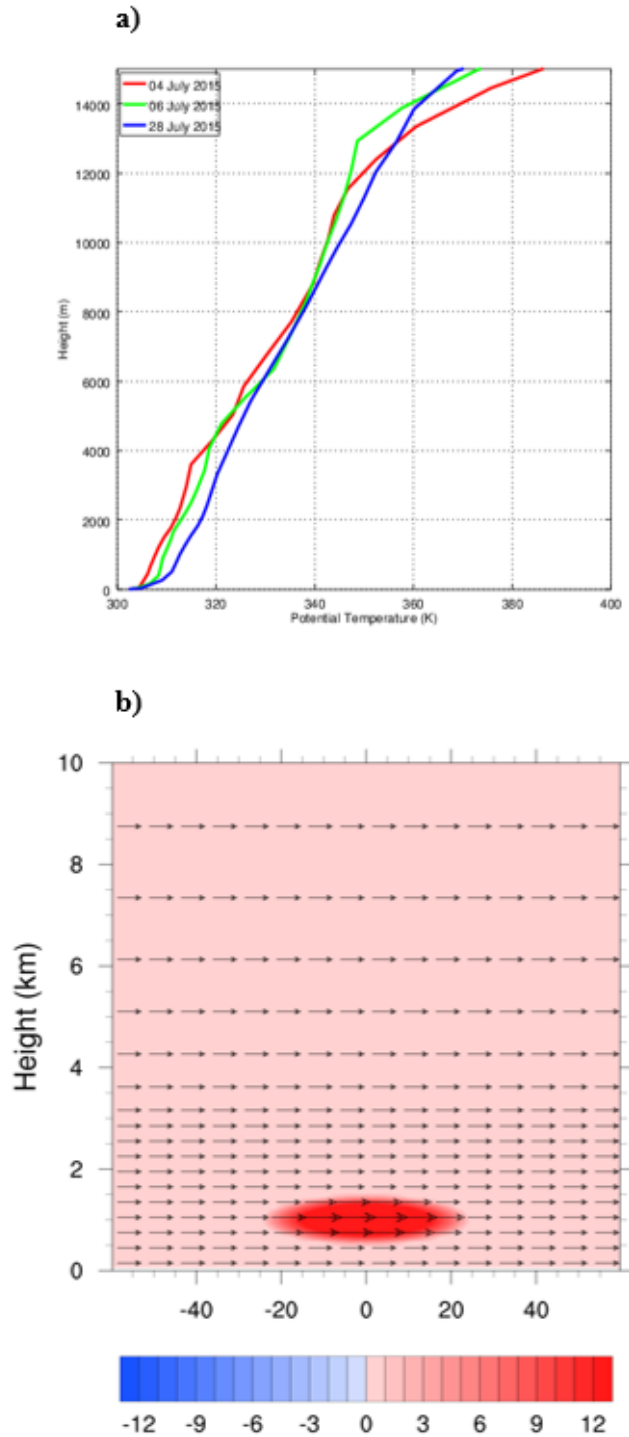


**Figure 13:** a) Potential temperature profiles at the starting time of three observed nocturnal convection cases. b) Initial wind profile of the simulations using the soundings in a) (note that the figure shows model domain depth only to 10 km, and the zonal winds in 10-15 km are the same as that in 8-10 km).

oscillation. Given that moisture tends to be greatest near the surface, the static stability will be slightly weaker in these profiles if moisture were included through virtual potential temperature.

In these cases, the model top is set to be at 15 km above the ground because the tropopause is well above the 10 km model top in the prior simulations. Observed winds were not used in the simulations. Instead, the winds are set identical to the jet simulations described in section 3b. As shown in Fig. 13b,  $u'$  in the jet has its peak intensity of  $20 \text{ ms}^{-1}$  at 1.0 km above the ground and decays to  $0 \text{ ms}^{-1}$  500 m both above and below the jet core following a quadratic function.

The simulated vertical motion using the temperature sounding at 0600UTC on 04 July 2015 and idealized wind profiles is shown in Fig. 14a. Results similar to Fig. 14a were also obtained from simulations of the cases 2 and 3 (not shown). Organized ascent develops from the near surface level to about 7.0 km over the jet. The strongest ascent of near  $1.0 \text{ ms}^{-1}$  is found on the eastern side of the jet from 1.5-2.0 km above ground level. Analyses of parcel trajectories and buoyancy have described processes consistent with those detailed in the previous vortex and jet simulations. Additional results from case 1, focusing on the sensitivity of these processes to the strength of the mean zonal westerly wind and the westerly wind perturbations arising from Coriolis torque on the GPLLJ, are shown in Figs. 14b and 14c. They share the same features revealed in Figs. 6, 7 and 12 for the vortex and jet simulations. These similar results from the simulations using observed temperature profiles and model resolutions help verify that the patterns of vertical motion and the mechanisms responsible for them are fairly robust.

#### 4. Summary and concluding remarks

We examined a process that could arise from the interactions of westerly zonal winds and the GPLLJ in the U.S. Great Plains during the midnight-early

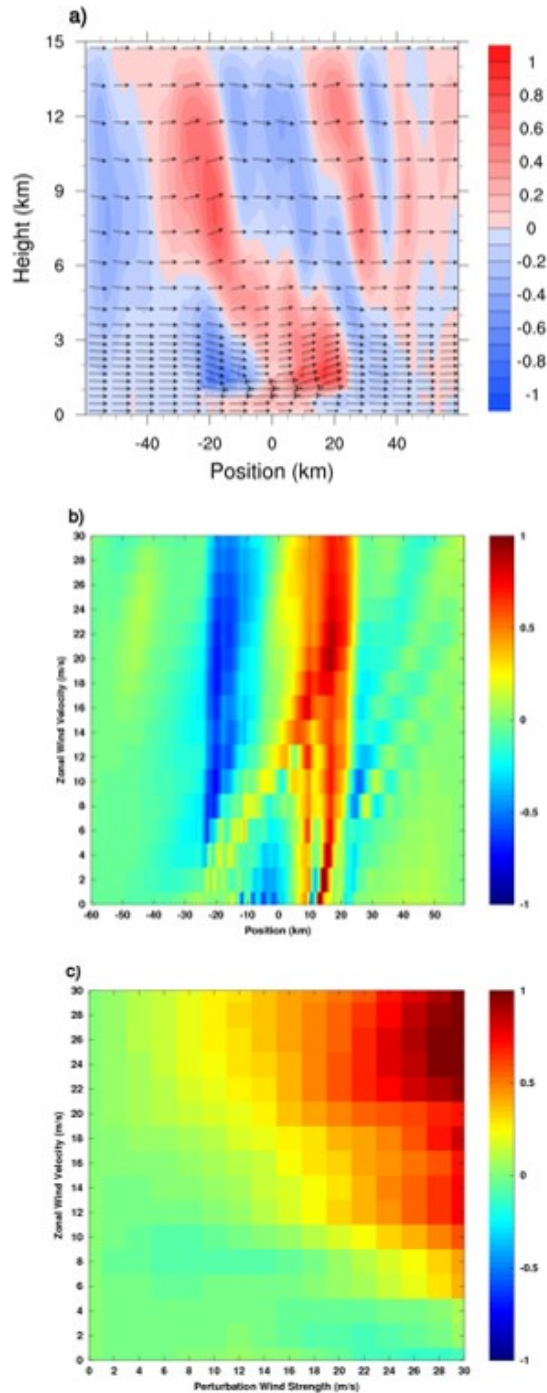


**Figure 14:** a) Vertical motion profile, b) vertical motion at 2 km above the ground level as functions of location from the domain center ( $x=0$ ) and mean westerly zonal wind ( $\bar{u}$ ), and c) vertical motion at 2 km above the ground level as functions of  $\bar{u}$  and jet intensity ( $u'$ ). All wind speeds have units of  $\text{ms}^{-1}$ .

morning hours in boreal spring and summer months, and could result in strong upward motion bearing resemblance to the observed vertical motion associated with initiation of nocturnal convection in the Great Plains. This process develops without requiring the presence of pre-existing air mass boundaries. Most of the recent studies and conceptual models of nocturnal CI in the Great Plains require either pre-existing boundaries or new CI in ongoing convection, e.g., upscale growth of thunderstorms (e.g., Trier et al. 2017). These boundaries provide persistent large-scale ascent, either directly (by convergence) or indirectly (through advection), that is essential to elevate air parcels to above the highly stratified atmosphere in the lowest 1 km and to ignite convection in the midnight-early morning hours. While elevated nocturnal convection initiated in the presence of boundaries accounts for one-half to two-third of observed cases in the Great Plains (Wilson and Roberts 2006; Reid and Bluestein 2017), the remainder occurred in the absence of boundaries and ongoing convection. By introducing and testing a process that can result in strong upward motion from intensifying interactions of the two dominant flow regimes in the Great Plains at night we may explain CI in events without boundaries.

As a first step to test this process we used two-dimensional ( $x$ - $z$ ) model simulations. In our modeling framework, interactions of the mean westerly zonal flow and the GPLLJ are described by a mean westerly flow and westerly wind perturbations in forms of 1) a boundary layer northern vortex and, in a more generalized case, 2) a low-level (1 km above the ground) westerly wind anomaly (jet). These westerly wind perturbations represent the  $u$ -momentum resulting from the Coriolis torque on an intense southerly GPLLJ at night. The main feature of vertical motions resulting from interactions of the two flow regimes is strong upward motion ( $\sim 1.0 \text{ ms}^{-1}$ ) on the eastern side of the northern vortex or jet. In vortex simulations, strong ascent further extends to the upper troposphere above the

vortex. In jet simulations, strong upward motion develops over the jet through the troposphere. There is also ascent in near-surface levels in both the vortex and jet simulations although the location and strength are different between them. Similar vertical motion profiles are found in our simulations when using NARR temperature profiles from three nocturnal CI cases.

Although differences exist in details of vertical motion profiles between the northern vortex and jet simulations, our parcel buoyancy analysis reveals a similar mechanism for the strong ascent on the eastern side of the perturbation westerly wind and above the perturbation in both settings. The perturbation westerly winds in the jet or the northern vortex (pertaining to the outcome of the Coriolis' effect on the GPLLJ) create divergence on the western side of the westerly wind perturbation and convergence on its eastern side. Air parcels above the divergence are mechanically forced downward, gaining positive buoyancy. Positively buoyant parcels rise above convergence on the eastern side, where the vertical pressure perturbation further contributes to the parcels' ascent. Sensitivity analysis shows that the buoyancy is larger when the westerly perturbation is stronger. Positive buoyancy also develops in the levels below the center of the northern vortex and the westerly perturbation center because of downward mechanical forcing by the vertical shear of the westerly perturbation. This mechanism produces ascent that may be sufficient for CI, but without the presence of air mass boundaries, moisture or latent heat. Some aspects of the interaction between the GPLLJ and the mean westerly flow are analogous to the aerodynamic lift described in the Kutta-Joukowski theorem although the absence of a rotating solid cylinder in our atmospheric simulations prevents direct comparisons. However, the theorem only describes lift generated through pressure perturbations produced by the interaction of a rotating cylinder with a passing laminar flow. As we have demonstrated, buoyancy-driven accelerations produce comparable vertical

accelerations to those driven by pressure perturbations in this situation. The theorem is frequently applied on smaller scales where buoyancy-driven accelerations are relatively unimportant compared to the effects of pressure perturbation. Because of the importance of buoyancy, any explanation of lift that relies solely on pressure perturbations will be incomplete, particularly in areas where the accelerations produced by pressure perturbations and buoyancy are in opposition, as is the case on the eastern flank of the vortex.

The vertical motion patterns from our simulations share many key features derived from observations of nocturnal convection in the U.S. Great Plains. Given that the southerly GPLLJ is coming perpendicular to the  $x$ - $z$  plane in our simulations, the organized band of strong ascent ( $\sim 1.0 \text{ ms}^{-1}$ ) on the east side of the northern vortex or the westerly anomaly (jet) in our simulations would be on the eastern flank of the GPLLJ and along its north-south orientation. This configuration of the GPLLJ and intense nocturnal convection has been reported in many observed cases (e.g., Hoecker 1963; Bonner 1968; Bonner et al. 1968; Mitchell et al. 1995; Whiteman et al. 1997; Song et al. 2005; Pu and Dickinson 2014; Reif and Bluestein 2017). The recent studies of Pu and Dickinson (2014) and Reif and Bluestein (2017) have also elaborated close associations of the GPLLJ with nocturnal CI occurring in the absence of boundaries.

Although the results of our two-dimensional numerical studies show strong ascent in the environment with a mean westerly zonal flow and low-level westerly perturbations resembling the effect of the Coriolis torque on the southerly GPLLJ, it remains puzzling why this ascent is not resolved in full-scale numerical models, even when they can simulate the GPLLJ (e.g., Ghan et al. 1996; DeMott et al. 2007; Stelten and Gallus 2017; Deng 2018). Stelten and Gallus (2017) examined the case of nocturnal convection on 6 July 2015 during PECAN. They noted that none of the convection-allowing WRF-based models that they

examined initiated convection that occurred in southeast Nebraska. Their comparisons of WRF versus NARR soundings from the same location and time revealed that the WRF models produced an inversion aloft and drier conditions than in the NARR. This could be explained by ascent being either under-forecasted or missed in those WRF simulations. Based on our idealized simulations, we propose that the likely failure to simulate the ascent may have been a result of the models' inaccuracy or inability to describe the westerly perturbations created by the Coriolis torque on the GPLLJ and their interactions with the mean westerly flow. This difficulty is apparently not alleviated by increasing model spatial resolution because some recent studies exploring the effect of model spatial resolution have dismissed any strong effect from further refining model grid (from 4 to 1 km) on nocturnal CI in cloud-resolving models (e.g., Thielen and Gallus 2019). Instead, our sensitivity analysis suggests a strong dependence of the ascent motion on description of the morphology (vertical and horizontal extent) and the strength of westerly perturbations resulting from the effect of the Coriolis torque on the southerly GPLLJ.

As faced by existing mechanisms proposed and being evaluated for nocturnal CI in the U.S. Great Plains (Shapiro et al. 2018), the processes that have been described and evaluated in this work need to be further tested. The advantage of this mechanism of strong ascent at night without air mass boundaries and moisture brings us an opportunity to understand the one-third of the population of nocturnal storms in the Great Plains that develop without such boundaries. Moreover, the demonstrated mechanical processes that can create strong lift in the atmospheric boundary layer and above add a new dimension in our pursuit of understanding atmospheric convection in general.

#### *Acknowledgements*

This study has been supported by the National Science Foundation grant AGS-

1924679 to the University of Nebraska. We thank the Holland Computing Center of the University of Nebraska for providing facilities and help during the numerical simulations of this work.

#### **References**

- Balling, R.C. Jr., 1985: Warm season nocturnal precipitation in the Great Plains of the United States. *J. Clim. Appl. Meteor.*, **24**, 1383-1387.
- Blackadar, A.K., 1957: Boundary layer wind maxima and their significance for the growth of nocturnal inversions. *Bull. Amer. Meteor. Soc.*, **38**, 283-290.
- Bonner, W.D., 1968: Climatology of the low-level jet. *Mon. Wea. Rev.*, **96**, 833-850.
- Bonner, W. D., S. Esbensen, and R. Greenberg, 1968: Kinematics of the low-level jet. *J. Appl. Meteor.*, **7**, 339-347.
- Bryan, G.H., and J.M. Fritsch 2000: Moist absolute instability: The sixth static stability state. *Bull. Amer. Meteor. Soc.*, **81**, 1207-1230.
- Bryan, G.H. and J.M. Fritsch, 2002: A benchmark simulation for moist nonhydrostatic numerical models. *Mon. Wea. Rev.*, **130**, 2917-2928.
- Coleman, T.A. and K.R. Knupp, 2011: Radiometer and profiler analysis of the effects of a bore and a solitary wave on the stability of the nocturnal boundary layer. *Mon. Wea. Rev.*, **139**, 211-223, doi.org/10.1175/2010MWR3376.1
- Corfidi, S.F., S.J. Corfidi, and D.M. Schultz, 2008: Elevated convection and castellanus: Ambiguities, significance, and questions. *Wea. Forecasting*, **23**, 1280-1330.
- Crighton, D.G., 1985: The Kutta condition in unsteady flow. *Ann. Rev. Fluid Mech.*, **17**, 411-445.
- Dai, A., 2001: Global precipitation and thunderstorm frequencies. Part II: Diurnal variations. *J. Clim.* **14**, 1112-1128.
- Dai, A., F. Giorgi, and K. E. Trenberth, 1999:

- Observed and model simulated precipitation diurnal cycle over the contiguous United States. *J. Geophys. Res.*, **104**, 6377–6402.
- DeMott, C.A., D.A. Randall, and M. Khairoutdinov, 2007: Convective precipitation variability as a tool for general circulation model analysis. *J. Clim.*, **20**, 91-111.
- Deng, X., 2018: *Evaluation of nocturnal convective precipitation over the Great Plains using reanalysis data and a WRF-based regional climate model*. MS Thesis, [available at] Department of Earth and Atmospheric Sciences, University of Nebraska-Lincoln. 52pp.
- French, A.J. and M.D. Parker, 2010: The response of simulated nocturnal convective systems to a developing low-level jet. *J. Atmos. Sci.*, **67**, 3384–3408, doi.org/10.1175/2010JAS3329.1
- Geerts, B., and coauthors, 2017: The 2015 Plains Elevated Convection at Night field project. *Bull. Amer. Meteor. Soc.*, **98**, 767-786.
- Ghan, S.J., X. Bian, and L. Corsetti, 1996: Simulation of the Great Plains low-level jet and associated clouds by general circulation models. *Mon. Wea. Rev.*, **124**, 1388-1408.
- Higgins, R.W., Y. Yao, E.S. Yarosh, J.E., Janowiak, and K.C. Mo, 1997: Influence of the Great Plains low-level jet on summertime precipitation and moisture transport over the central United States. *J. Clim.*, **10**, 481-507.
- Hoecker, W. H., 1963: Three southerly low-level jet systems delineated by the Weather Bureau special pibal network in 1961. *Mon. Wea. Rev.*, **91**, 573–582.
- Holton, J. R., 1967: The diurnal boundary layer wind oscillation above sloping terrain. *Tellus*, **19**, 199-205.
- Holton, J.R., and G.J. Hakim, 2013: *An Introduction to Dynamic Meteorology*, Chapters 4 and 6. Academic Press.
- Kincer, J. B., 1916: Daytime and nighttime precipitation and their economic significance. *Mon. Wea. Rev.*, **44**, 628-633.
- Liu, C., and M.W. Moncrieff, 1996: A numerical study of the effects of ambient flow and shear on density currents. *Mon. Wea. Rev.*, **124**, 2282-2303.
- Marshall, J.H., S.B. Trier, T.M. Weckwerth, and J.W. Wilson, 2011: Observations of elevated convection initiation leading to a surface-based squall line during 13 June IHOP\_2002. *Mon. Wea. Rev.*, **139**, 247–271, doi.org/10.1175/2010MWR3422.1
- Mesinger, F., and coauthors, 2006: North American regional reanalysis. *Bull. Amer. Meteor. Soc.*, **87**, 343-360.
- Milne-Thompson, L.M., 1972: *Theoretical Hydrodynamics*. Macmillan, London, 200-202pp.
- Mitchell, M. J., R. W. Arritt and K. Labas, 1995: A climatology of warm season Great Plains low-level jet using wind profiler observations. *Wea. Forecasting*, **10**, 576–591.
- Pu, B., and R. E. Dickinson, 2014: Diurnal spatial variability of Great Plains summer precipitation related to the dynamics of the low-level jets. *J. Atmos. Sci.*, **71**, 1807–1817.
- Rasmusson, E.M., 1967: Atmospheric water vapor transport and the water balance of North America. Part I: Characteristics of the water vapor flux field. *Mon. Wea. Rev.*, **95**, 403–426.
- Reif, D.W., and H.B. Bluestein, 2017: A 20-year climatology of nocturnal convection initiation over the central and southern Great Plains during the warm season, *Mon. Wea. Rev.*, **145**, 1615-1639.
- Shapiro, A., E. Fedorovich, J.G. Gebauer, 2018: Mesoscale ascent in nocturnal low-level jets. . *J. Atmos. Sci.*, **75**, 1403-1427, doi: 10.1175/JAS-D-17-0279.1
- Song, J., K. Liao, R.L. Coulter, and B.M. Lesht, 2005: Climatology of the low-

- level jet at the southern Great Plains atmospheric boundary layer experiments site. *J. Appl. Meteor.*, **44**, 1593–1606, doi.org/10.1175/JAM2294.1
- Stelten, S. and W.A. Gallus, 2017: Pristine nocturnal convective initiation: A climatology and preliminary examination of predictability. *Wea. Forecasting*, **32**, 1613–1635.
- Thielen, J.E., and W.A. Gallus, Jr., 2019: Influences of horizontal grid spacing and microphysics on WRF forecasts of convective morphology evolution for nocturnal MCSs in weakly forced environments. *Wea. Forecasting*, **34**, 1495-1517.
- Trier, S.B., J.W. Wilson, D.A. Ahijevych, and R.A. Sobash, 2017: Mesoscale vertical motions near nocturnal convection initiation in PECAN. *Mon. Wea. Rev.*, **145**, 2919-2941.
- Wallace, J. M., 1975: Diurnal variations in precipitation and thunderstorm frequency over the conterminous United States. *Mon. Wea. Rev.*, **103**, 406-419.
- Whiteman, C. D., X. Bian, and S. Zhong, 1997: Low-level jet climatology from enhanced rawinsonde observations at a site in the southern Great Plains. *J. Appl. Meteor.*, **36**, 1363–1376, doi.org/10.1175/1520-0450(1997)036<1363:LLJCFE>2.0.CO;2
- Wilson, J. W., and R. D. Roberts, 2006: Summary of convective storm initiation and evolution during IHOP: Observational and modeling perspective. *Mon. Wea. Rev.*, **134**, 23–47.
- Wilson, J.W., S.B. Trier, D.W. Reif, R.D. Roberts, and T.M. Weckwerth, 2018: Nocturnal elevated convection initiation of the PECAN 4 July hailstorm. *Mon. Wea. Rev.*, **146**, 243–262, doi.org/10.1175/MWR-D-17-0176.1
- Wu, Q., and M.W. Moncrieff, 1994: Density current circulations in shear flows. *J. Atmos. Sci.*, **51**, 511-524.
- Zhang, G., 2003: Roles of tropospheric and boundary layer forcing in the diurnal cycle of convection in the U.S. southern great plains. *Geophys. Res. Lett.*, **30**, doi:10.1029/2003GL018554, 2003